

Uncovering genomic trajectories with heterogeneous genetic and environmental backgrounds across single-cells and populations

Kieran R Campbell^{1,2} and Christopher Yau^{*2,3}

¹Department of Physiology, Anatomy and Genetics, University of Oxford, Oxford, UK

²Wellcome Trust Centre for Human Genetics, University of Oxford, Oxford, UK

³Centre for Computational Biology, Institute of Cancer and Genomic Sciences, University of Birmingham,
Birmingham, UK

July 5, 2017

Abstract

Pseudotime algorithms can be employed to extract latent temporal information from cross-sectional data sets allowing dynamic biological processes to be studied in situations where the collection of genuine time series data is challenging or prohibitive. Computational techniques have arisen from areas such as single-cell 'omics and in cancer modelling where pseudotime can be used to learn about cellular differentiation or tumour progression. However, methods to date typically assume homogenous genetic and environmental backgrounds, which becomes particularly limiting as datasets grow in size and complexity. As a solution to this we describe a novel statistical framework that learns pseudotime trajectories in the presence of non-homogeneous genetic, phenotypic, or environmental backgrounds. We demonstrate that this enables us to identify interactions between such factors and the underlying genomic trajectory. By applying this model to both single-cell gene expression data and population level cancer studies we show that it uncovers known and novel interaction effects between genetic and environmental factors and the expression of genes in pathways. We provide an R implementation of our method *PhenoPath* at <https://github.com/kieranrcampbell/phenopath>.

*c.yau@bham.ac.uk

25 Introduction

26 Dynamic or progressive biological behaviours are ideally studied within a longitudinal framework
27 that allows for monitoring of individuals over time leading to direct time course data. However,
28 longitudinal studies are often challenging to conduct and cohort sizes limited by logistical and
29 resource availability. In contrast, cross-sectional surveys of a population are often relatively easier to
30 conduct in large numbers and are more prevalent for molecular 'omics based studies. Cross-sectional
31 studies do not directly capture the changes in disease characteristics in patients but it maybe possible
32 to recapitulate aspects of temporal variation by applying “pseudotime” computational analysis.

33 The objective of pseudotime analysis is to take a collection of high-dimensional molecular data
34 from a cross-sectional cohort of individuals and to map these on to a series of one-dimensional
35 quantities, that are called *pseudotimes*. These pseudotimes measure the relative progression of
36 each of the individuals along the biological process of interest, e.g. disease progression, cellular
37 development, etc., allowing us to understand the (pseudo)temporal behaviour of measured features
38 without explicit time series data (Figure 1A). This analysis is possible when individuals in the cross-
39 sectional cohort behave asynchronously and each is at a different stage of progression. Therefore,
40 by creating a relative ordering of the individuals, we can define a series of molecular states that
41 constitute a *trajectory* for the process of interest.

42 Pseudotime methods generally rely on the assumption that any two individuals with similar
43 observations should carry correspondingly similar pseudotimes and algorithms will attempt to find
44 some ordering of the individuals that satisfies some overall global measure that best adheres to
45 this assumption (Figure 1A). Exact implementations and specifications differ between pseudotime
46 approaches particularly in the way “similarity” is defined and modelled. When applied to molecular
47 data, pseudotime analysis typically captures some dominant mode of variation that corresponds to
48 the continuous (de)activation of a set of biological pathways [Fan et al., 2016].

49 Pseudotime analysis has gained great popularity in the domain of single cell gene expression
50 analysis (where each “individual” is now a single cell) in which it has been applied to model the
51 differentiation of single-cells [Trapnell et al., 2014, Reid and Wernisch, 2016, Haghverdi et al., 2016,
52 Campbell and Yau, 2016, Setty et al., 2016]. Using advanced machine learning techniques, these
53 methods can be applied to characterise complex, nonlinear behaviours, such as cell cycle, and mod-
54 elling branching behaviours to allow, for example, the possibility of cell fate decision making. His-
55 torically, single cell applications were pre-dated by more general applications in modelling cancer
56 progression from gene expression profiling of tumours [Qiu et al., 2011, Magwene et al., 2003, Gupta
57 and Bar-Joseph, 2008] as well as in other progressive disease contexts such as glaucoma [Tucker and
58 Garway-Heath, 2010, Tucker et al., 2017, Tucker and Li, 2015, Tucker et al., 2015]. However, to
59 date, there has been little cross-over between these domains in terms of methodological development
60 due to the differing contexts in which methods are applied.

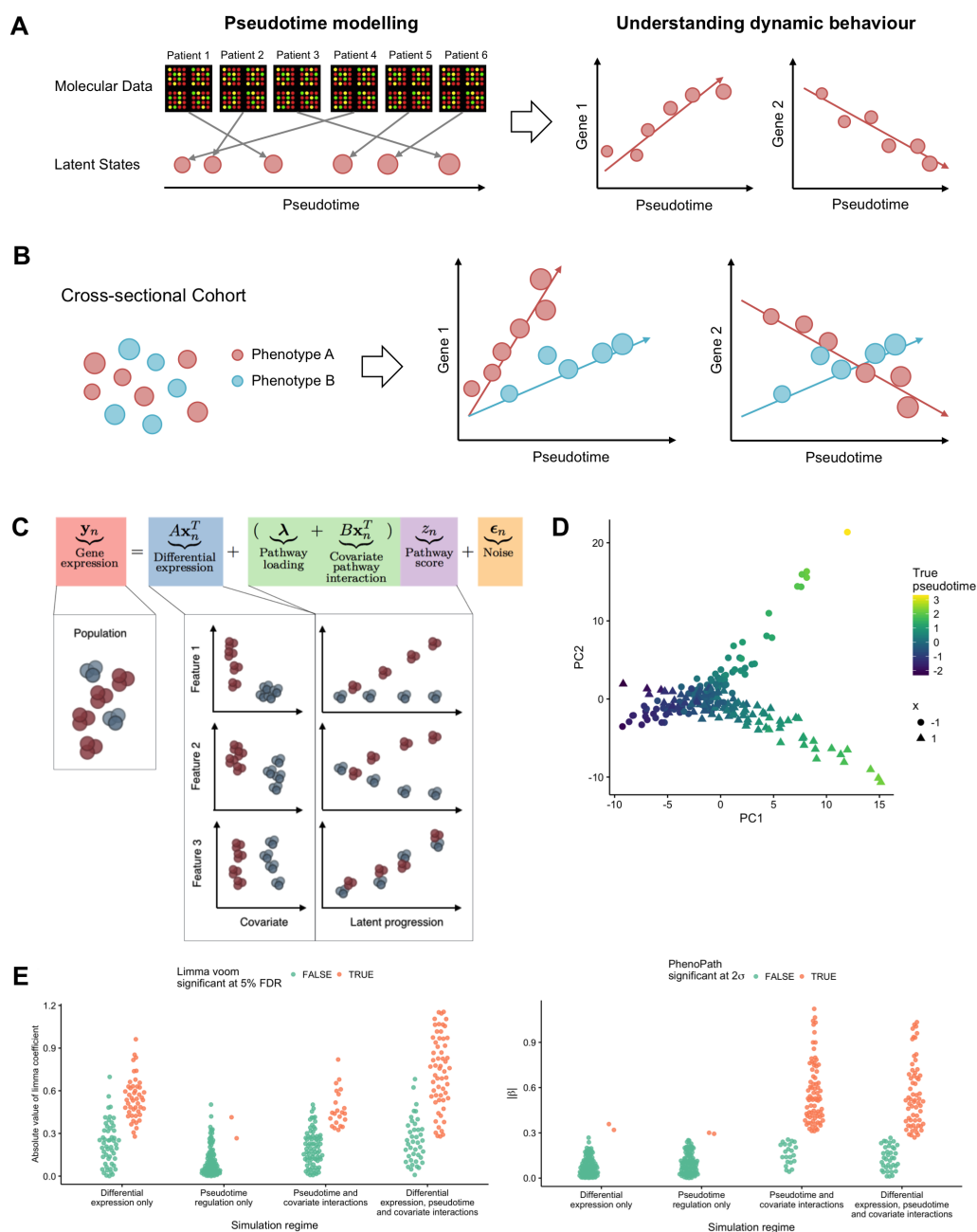


Figure 1: **Pseudotemporal analysis.** **A** High-dimensional molecular data from a cross-sectional cohort is mapped on to a one-dimensional pseudotemporal progression scale allowing pseudotemporal behaviour of individual features to be analysed. **B** If the cohort contains sub-populations we may want each sub-population to be associated to distinct trajectories. **C** PhenoPath models observed expression as a combination of standard differential expression and pseudotime/pathway effects, including covariate-pathway interactions. **D** PCA representation of a simulated dataset coloured by pseudotime shows a clear splitting of trajectories between covariate status $x = (-1, 1)$. **E** Simulation results showing the absolute value of the effect size reported by limma voom and the interaction coefficients β reported by PhenoPath under the four different simulation regimes and coloured by significance at 5% FDR.

61 For instance, a limitation of pre-existing pseudotime approaches is that they generally do not
62 provide a mechanism to account for known genetic, phenotypic and environmental information that
63 might allow us to answer questions related to the interaction between heterogeneity in these factors
64 and pseudotime progression. For example, do immune cells exposed to different stimuli progress
65 differently in their response? Do the transcriptional programmes of tumours differ based on mutation
66 status of a known cancer gene? Whilst pseudotime methods exist for unsupervised identification of
67 multiple or branching pseudotime trajectories, these can only be *retrospectively* examined for their
68 association with external factors of interest and do not provide an explicit approach for identifying
69 associations.

70 In this paper, we describe a novel Bayesian statistical framework for pseudotime trajectory
71 modelling to address these limitations. Our framework models global pseudotemporal progression
72 but incorporates covariates that can modulate the pseudotemporal progression allowing sub-groups
73 within the cross-sectional population to each develop their own trajectory (Figure 1B). Our approach
74 combines linear regression and latent variable modelling approaches and allows for interactions be-
75 tween the covariate and temporally driven components of the model. We believe our method to
76 be the first integrated statistical approach for modelling pseudotime trajectories against heteroge-
77 neous genetic and environmental backgrounds allowing its utility in both single and non-single cell
78 applications.

79 Results

80 **PhenoPath: a Bayesian statistical framework for learning continuous path- 81 way or pseudotemporal with covariates**

82 We first give an overview of our statistical method which we call “PhenoPath”. For simplicity, our
83 descriptions will assume that the observed data are high-dimensional gene expression measurements
84 which are used throughout our empirical experiments but we stress that the model would be appli-
85 cable to a wider range of data modalities. PhenoPath uses a Bayesian statistical framework that
86 combines linear regression and latent variable modelling. The observed data (\mathbf{y}_n) for the n -th indi-
87 vidual is a linear function of both measured covariates (\mathbf{x}_n) and an unobserved latent variable (z_n)
88 corresponding to pseudotime. We will also refer to this latter quantity more generically as a *path-
89 way score* since, as we will explore further, pseudotime progression will be driven by the activities
90 of certain biological pathways. Figure 1C shows a schematic of the model. The covariate-dependent
91 component ($A\mathbf{x}_n$) models differential expression whilst the pseudotime component involves both a
92 pathway-only component ($\boldsymbol{\lambda}$). The key novelty is an interaction term ($B\mathbf{x}_n^T z_n$) that allows the the
93 covariates to modulate the pathway or pseudotemporal trajectory. We devise a Bayesian hypothesis
94 test for the model to test for these interaction effects (see Methods for details). An attractive fea-

95 ture of the framework is that, in the absence of pseudotemporal variation, the model reduces to a
96 standard differential expression model. Whilst, in the absence of measured covariates, it is a factor
97 analysis latent variable model for pseudotime.

98 In our investigations, the covariates will be discrete, binary quantities but this is not a necessary
99 restriction. Sparse Bayesian prior probability distributions are used to constrain the parameters
100 (A, B, λ) so that covariates only drive the emergence of distinct trajectories only if there is sufficient
101 information within the data to do so. Computational inference within PhenoPath is handled by
102 a fast and highly scalable variational Bayesian inference framework that can handle thousands of
103 features and samples in minutes using a standard personal computer making it readily applicable to
104 large data sets without the use of high-performance computing (see Methods for details).

105 **Simulation study**

106 We first demonstrate the utility of our model by performing a simulation study to demonstrate
107 the value of modelling covariate-pathway interactions. We simulated RNAseq-based gene expres-
108 sion data [Frazee et al., 2015] where genes were either (1) differentially expressed only, (2) exhibiting
109 pseudotime progression only, (3) driven by covariate-modulated pseudotime progression, or (4) differ-
110 entially expressed with covariate-modulated pseudotime progression (see Methods for details, Figure
111 1D, Supplementary Fig. 1). PhenoPath exhibited high specificity and sensitivity by classifying only
112 a small number of simulated genes (2%) as exhibiting interaction effects in cases 1-2 where there
113 are no covariate-pseudotime interactions but identifies 78% and 63% of genes as exhibiting signif-
114 icant covariate-pseudotime interactions in cases 3 and 4 respectively (Fig. 1E). For comparison, a
115 standard differential expression analysis using limma-voom identified 47% and 59% of genes as dif-
116 ferentially expressed in cases 1 and 4 respectively. In case 2 only 2% of genes are identified as DE as
117 expected but, in case 3, 22% of genes are identified as DE where limma-voom would not be expected
118 to report any differentially expressed genes. We sought to compare the performance of Limma Voom
119 and PhenoPath in detecting differential expression and pathway interaction effects respectively, and
120 show that there are pathway interaction effects not evident from differential expression analyses
121 alone. We found that PhenoPath identifies such interactions with high precision (Supplementary
122 Table 1).

123 **Single-cell RNA-seq perturbation analysis**

124 We next examined a time-series single-cell RNA-seq (scRNA-seq) data set of bone marrow derived
125 dendritic cells responding to particular stimuli [Shalek et al., 2014]. Cells were exposed to LPS,
126 a component of Gram-negative bacteria, and PAM, a synthetic mimic of bacterial lipopeptides,
127 and scRNA-seq performed at 0, 1, 2, 4 and 6 hours after stimulation. Despite the time-series
128 measurement, previous studies have suggested this dataset is more suited to a “pseudotime” analysis

129 as the cells respond asynchronously and heterogeneity exists within the cellular populations at each
130 time point [Reid and Wernisch, 2016]. To-date pseudotime inference algorithms would typically
131 assume a common trajectory across all experimental conditions or a pseudotime analysis performed
132 separately for each stimulant. This might give a loss of statistical power and artefacts introduced by
133 confounding effects. Using our model we can encode the stimulant to which the cells were exposed as
134 a covariate and allow gene expression to evolve along pseudotime differently for either LPS or PAM
135 exposure. This allows us to learn a single trajectory for all cells regardless of stimulant applied yet
136 simultaneously infer which genes are differentially regulated in response. We applied this to the 820
137 cells exposed to LPS and PAM in the time points 1, 2, 4, and 6 hours after stimulation using the
138 7,533 genes whose variance in normalised log-expression exceeded a pre-set threshold (see Methods
139 for details).

140 We inferred a covariate-perturbed trajectory and uncovered a landscape of pseudotime-stimulant
141 interactions (Fig. 2A), unveiling genes whose regulation along pseudotime is modulated by the appli-
142 cation of LPS or PAM. The trajectory inferred largely recapitulated the true time-series measurement
143 (Fig. 2B, $R^2 = 0.64$), despite no explicit temporal information being provided to the algorithm,
144 though transcriptional heterogeneity at each time point is still evident. We also compared this to two
145 commonly-used pseudotime algorithms and found that the pseudotimes inferred using PhenoPath
146 had the best agreement with the capture times (Supplementary Fig. 2), possibly due to the ability
147 to integrate the confounding effect of differential stimulant exposure.

148 Using PhenoPath we discovered a large number of stimulant-modulated interactions masked by
149 standard differential-expression analysis (Fig. 2C). A GO analysis revealed genes whose upregulation
150 along the common trajectory was increased by LPS exposure (as opposed to PAM) were highly
151 enriched for interferon-beta and immune response (Fig. 2D), which recapitulates previous results
152 [Shalek et al., 2014, Reid and Wernisch, 2016] that suggest a “core” module of antiviral genes
153 upregulated at later timepoints in LPS cells but in an entirely unsupervised, integrated manner.
154 We finally examined the individual genes most perturbed by LPS or PAM along the trajectory
155 (Fig. 2E), which identifies as yet uncharacterised expression patterns associated with LPS and
156 PAM. Most notably, the tumour necrosis factor *Tnf* had around twice the interaction effect size
157 of any other gene, and decreases under LPS stimulation but increases under PAM. Further genes
158 exhibit differential regulation according to stimulant, such as *Mef2c* that has constant expression
159 over pseudotime under LPS stimulation yet shows downregulation under PAM stimulation. These
160 results complement previously discovered gene differences such as that of *Tnf*, but in a systematic,
161 transcriptome-wide approach.

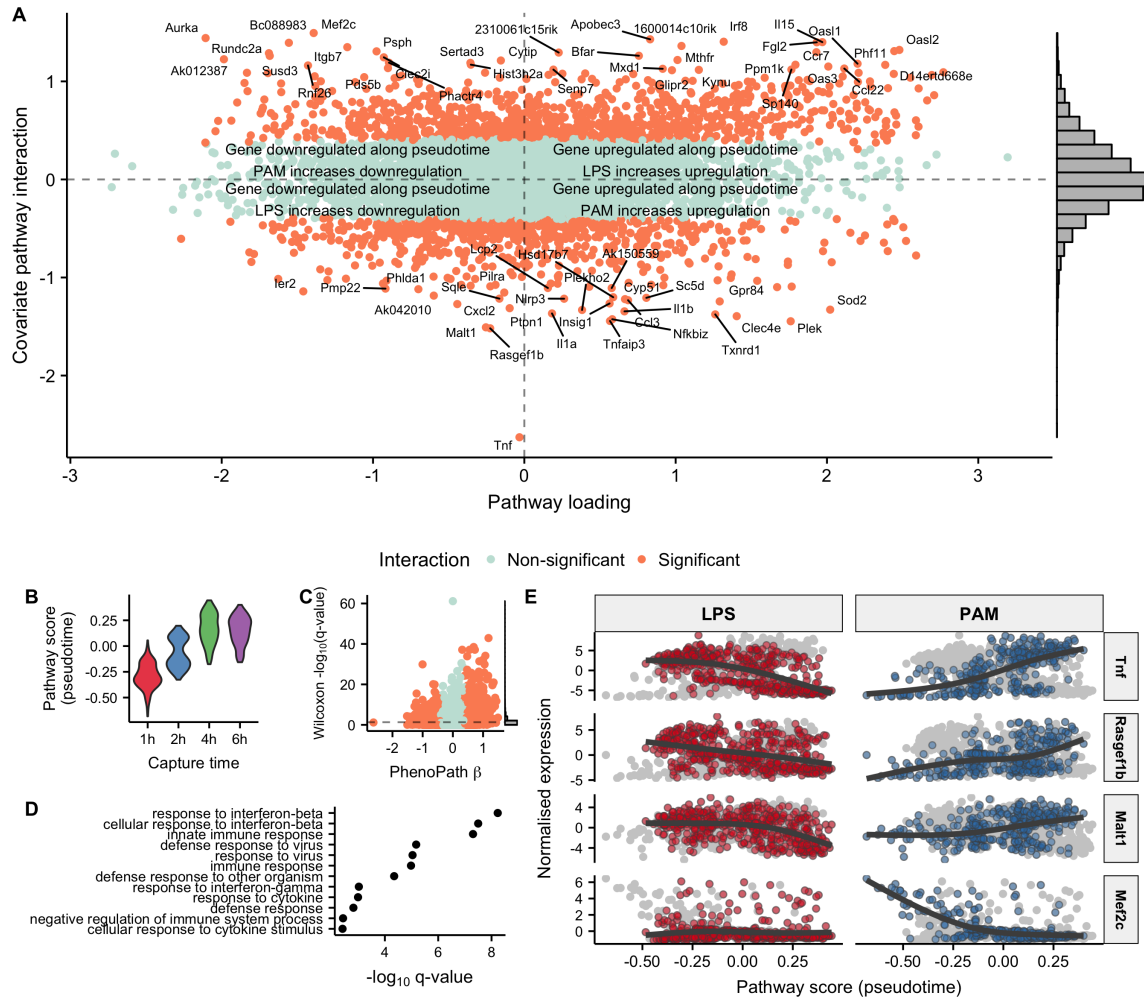


Figure 2: Stimulant-immune reactions in single-cell RNA-sequencing data. **A** PhenoPath applied to the Shalek et al. dataset uncovers genes differentially regulated along pseudotime depending on the stimulant (LPS or PAM) applied. **B** The inferred pseudotimes (z) consistent with the physical capture times. **C** A comparison of p -values obtained through a nonparametric statistical test for differential expression between LPS and PAM stimulation shows no particular relation with the interaction parameters β inferred with PhenoPath. **D** A GO enrichment analysis of the genes upregulated along pseudotime whose upregulation was increased by LPS stimulation showed enrichment for immune system processes. **E** Expression of the four genes with the largest interaction effect sizes along over pseudotime, stratified by stimulant applied. Strikingly, *Tnf* is upregulated under PAM exposure yet downregulated under LPS stimulation.

162 Identifying microsatellite instability associated gene expression hetero- 163 geneity in colorectal cancer

164 We next applied our model to a non-single cell setting by examining RNA-seq gene expression data
165 from the TCGA colorectal adenocarcinoma (COAD) cohort [Network et al., 2012]. We used mi-
166 crosatellite instability status (MSI) as a phenotypic covariate and wanted to identify pseudotemporal
167 expression patterns associated with MSI status. MSI is genetic hypermutability that is present in
168 around 15% of colorectal tumours and is associated with differential response to chemotherapeutics
169 and marginally improved prognosis [Boland and Goel, 2010].

170 We applied PhenoPath to 4,801 highly variable genes across 284 samples to identify a pseu-
171 dotemporal trajectory through these tumours (see Methods for details). This analysis uncovered a
172 landscape of 92 pathway-MSI interactions including known tumour suppressor genes (Fig. 3A &
173 Supplementary Data 1). Patients further advanced along the trajectory exhibited higher expres-
174 sion of T regulatory cell (Tregs) immune markers (Fig. 3B) likely due to increasing T regulatory
175 cell infiltration of the tumour. This led us to hypothesise that the inferred pseudotime trajectory
176 corresponds to immune response pathway activation in the tumours, further supported by a Gene
177 Ontology (GO) enrichment analysis for genes upregulated along the trajectory (Fig. 3C). Tumour-
178 infiltrating Tregs are potent immunosuppressive cells of the immune system that promote progression
179 of cancer through their ability to limit antitumour immunity and promote angiogenesis and often
180 associated with a poor clinical outcome [Facciabene et al., 2012]. A standard differential expression
181 analysis using limma voom [Law et al., 2014] (Fig. 3D) demonstrates that PhenoPath is required
182 to uncover such interactions as a gene being differentially expressed does not imply a pathway-MSI
183 interaction, while such interactions do not require differential expression.

184 The most striking interaction discovered for this dataset was the *MLH1* gene whose interaction
185 effect size was far larger than any other gene. This association provided a positive control since
186 *MLH1* is a DNA mismatch repair gene and germline mutations of which are causal for hereditary
187 non-polyposis colorectal cancer [Bonadona et al., 2011, Gille et al., 2002]. By applying PhenoPath we
188 correctly identified that in patients, with low or absent levels of microsatellite instability, there is no
189 relationship between *MLH1* expression and immune pathway interaction, with *MLH1* expressed at
190 an approximately constant level (Fig. 3E). However, when MSI occurs in a tumour, *MLH1* expression
191 is highly correlated with immune response, showing almost no expression when the immune pathway
192 is inactive and gradually being upregulated with immune pathway response [Michel et al., 2008].

193 Tracking ER modulated angiogenesis driven progression in breast cancer

194 We next performed a pseudotemporal analysis of the TCGA breast cancer cohort using estrogen
195 receptor (ER) status as a phenotypic covariate. Approximately 60% of breast cancers are estrogen

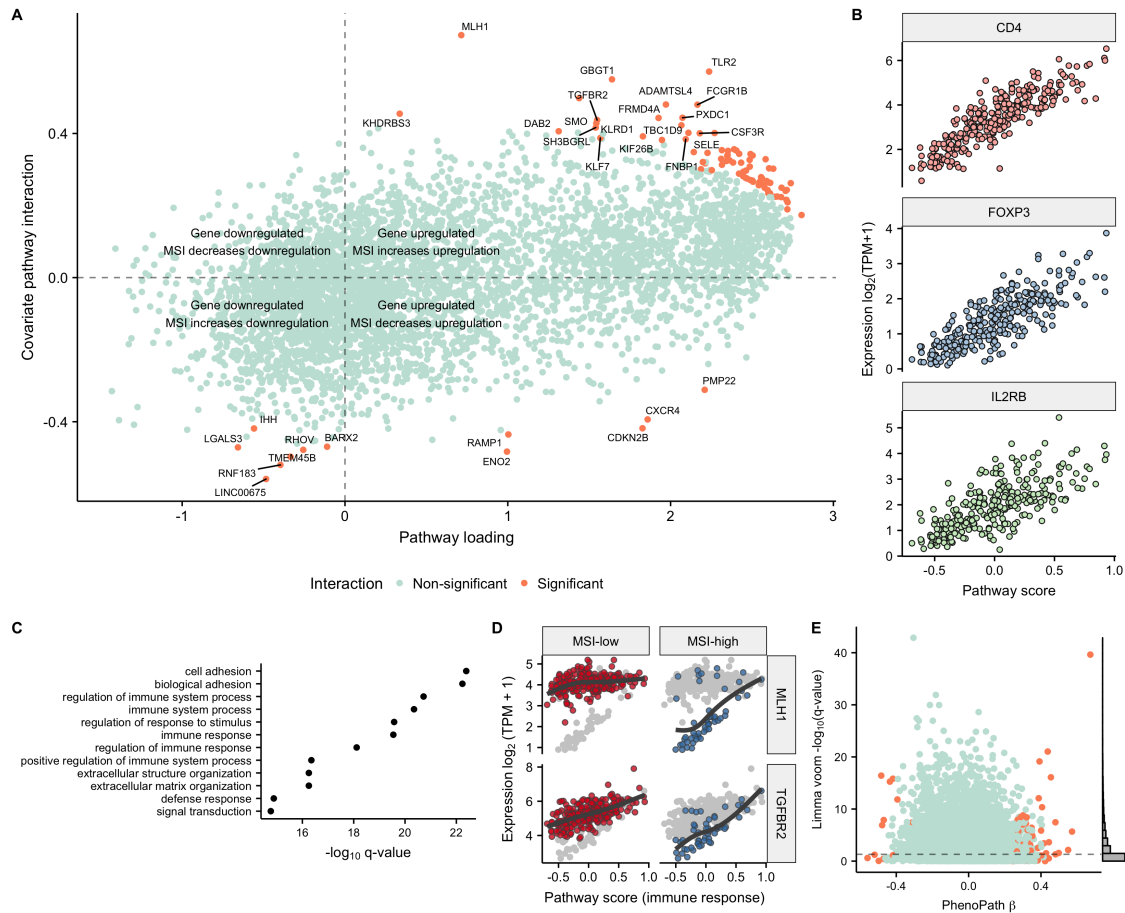


Figure 3: Immune-microsatellite instability interactions uncovered in colorectal adenocarcinoma. **A** PhenoPath applied to colorectal adenocarcinoma (COAD) RNA-seq expression data uncovers a landscape of interactions between the inferred immune trajectory and microsatellite instability status (MSI). **B** Expression of three T regulatory cell markers demonstrates that our pseudotime corresponds to activation of immune response pathways. **C** A comparison to the FDR-corrected q -values reported by Limma Voom demonstrates genes found interacting with MSI status and the immune pathway are found to be both DE and non-DE in standard analyses. **D** A GO enrichment analysis of upregulated genes implies the latent trajectory encodes immune pathway activation in each tumour. **E** The tumour suppressor genes *MLH1* and *TGFBR2* were identified by our method as being significantly perturbed along the immune trajectory by MSI status. *MLH1* shows no interaction with immune pathway activation in the MSI-low regime yet is highly correlated with immune pathway activation in the MSI-high regime.

196 receptor positive [Early Breast Cancer Trialists' Collaborative Group (EBCTCG)], which is typically
197 associated with improved prognosis and a longer time to recurrence [Parl et al., 1984]. We applied
198 PhenoPath to 1,135 samples post-QC and 4,579 highly variable genes (see Methods for details).
199 Using stringent significance testing threshold we found 1,932 genes (42%) affected by an interaction
200 between the pseudotemporal trajectory and ER receptor status (Fig. 4E & Supplementary Data 2).
201 There was a correlation between the pathway interaction strength and the p -value reported through
202 standard differential expression (Fig. 4B), though there remained some genes that exhibited pathway
203 interaction and no differential expression.

204 A GO enrichment analysis indicated that the inferred pseudotemporal trajectory corresponded
205 to vascular growth pathways or *angiogenesis* (Fig. 4F) – a well-known and uncontroversial hallmark
206 of cancer development [Ferrara, 2002, Welts et al., 2013]. We confirmed this finding by specifically
207 examining the expression of known angiogenesis inducing genes (Supplementary Fig. 4). We found
208 increasing fibroblast growth factor-2 (*FGF-2*) and vascular endothelial growth factors C and D
209 (*VEGF-C/D*) expression along the trajectory whose behaviours were independent of ER status.

210 We finally sought to examine the genes identified as being most affected by the interaction
211 between angiogenesis and estrogen receptor status. Importantly, this set included the Estrogen
212 Receptor 1 (*ESR1*) gene as well as the forkhead transcription factors *FOXA1* and *FOXC1* which
213 are known to be involved with ER α mediated action in breast cancer [Lam et al., 2013, Yu-Rice
214 et al., 2016] (Fig. 4D and Supplementary Fig. 3). Fig. 4D shows how the fructose-1,6-biphosphatase
215 (*FBP1*) and *FOXC1* genes evolve along the angiogenesis pathway dependent on ER status. In the
216 ER- regime, *FBP1* is upregulated along the trajectory while in the ER+ regime it is downregulated.
217 Intriguingly, *FBP1* has been identified as a marker to distinguish ER+ from ER- subtypes and its
218 expression has been shown to be negatively correlated with *SNAIL* as the Snail-G9a-Dnmt1 complex,
219 is critical for E-cadherin promoter silencing, and required for the promoter methylation of FBP1 in
220 basal-like breast cancer [Dong et al., 2013] (Supplementary Fig. 5). Similarly, *FOXC1* shows no
221 regulation in the ER- regime yet is strongly upregulated in the ER+ case.

222 We noted that these genes exhibit a convergence - they have markedly different expression at
223 the beginning of the trajectory based on ER status yet converge towards the end. We derived a
224 mathematical formula to infer such convergence points and calculated these for all genes showing
225 significant interactions (see Methods for details). Remarkably, the vast majority converge towards
226 the end of the trajectory (Fig. 4E), implying a common end-point in vascular development for
227 both ER+ and ER- cancer subtypes (Supplementary Fig. 6). This effect can be seen in the example
228 expression plots in Figure 4D, where the vertical dashed line represents the convergence point always
229 at the end of the trajectory. This suggests that while there exists low levels of angiogenesis pathway
230 activation, ER status dominates gene expression while as angiogenesis pathway activation increases
231 it comes to dominate expression patterns over ER status. This finding might have implications for

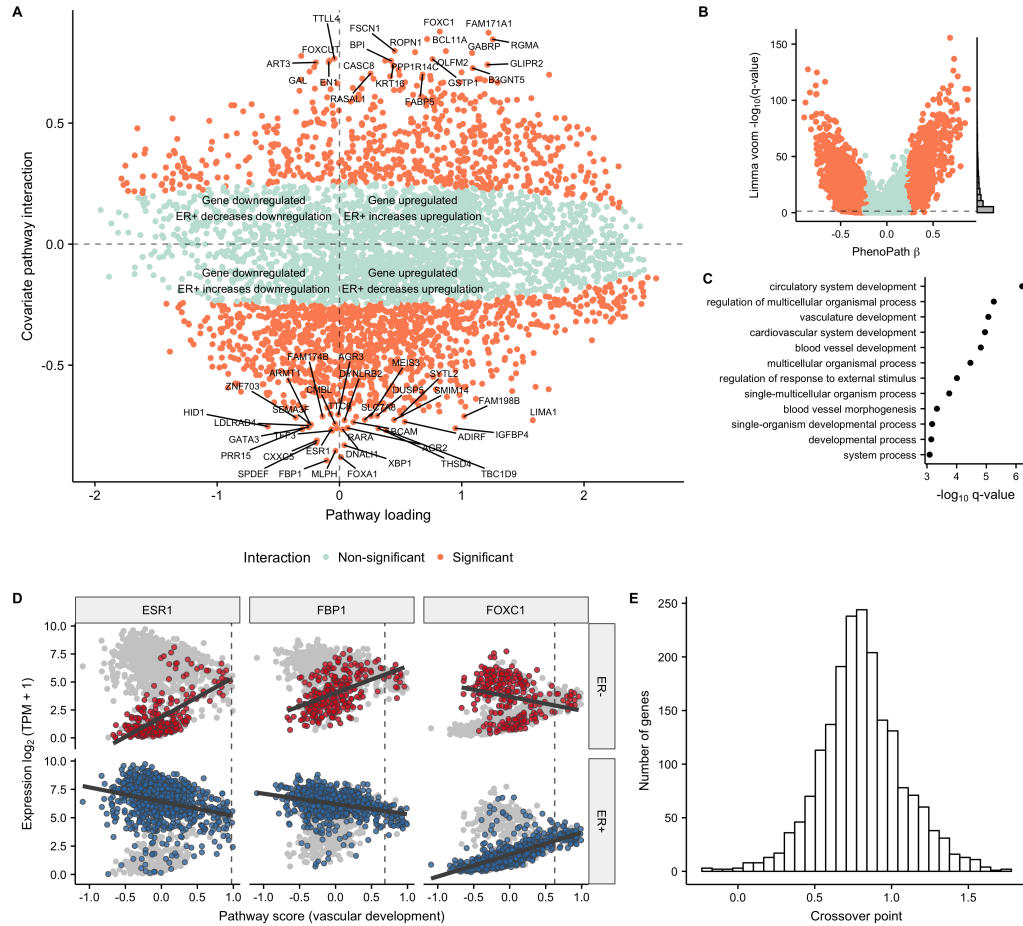


Figure 4: Vascular growth-ER status interactions uncovered by PhenoPath in breast cancer. **A** PhenoPath applied to Breast Cancer (BRCA) RNA-seq expression data uncovers a landscape of interactions between the inferred angiogenesis trajectory and estrogen receptor (ER) status. **B** A comparison to the FDR-corrected q -values reported by Limma Voom identifies a significant number of DE genes display an interaction with ER status and the angiogenic pathway. **C** A GO enrichment analysis of upregulated genes implies the latent trajectory encodes angiogenesis pathway activation in each tumour. **D** Four example genes *ESR1*, *FBP1*, and *FOXC1* were identified by PhenoPath as significantly perturbed along the angiogenesis trajectory by ER status. The vertical dashed line signifies the calculated crossover point, demonstrating the expression profiles of these genes converge towards the end of the trajectory. **E** A histogram of the crossover points of all genes whose trajectory-covariate interactions were significant. The vast majority of crossover points are at the end of the trajectory (around 0.5, where the “middle” pathway score is 0) implying a convergence of gene expression as the trajectory progresses.

232 the application of angiogenesis inhibitors in breast cancer treatment.

233 Discussion

234 PhenoPath provides a novel contribution to the pre-existing arsenal of pseudotemporal analysis
235 algorithms developed across a range of application areas including single cell 'omics and cancer. Us-
236 ing a statistical model that allows for covariate-modulated pseudotemporal trajectories, PhenoPath
237 generalises pseudotime analysis to a wider range of applications where genetic, phenotypic or en-
238 vironmental contexts may vary between samples and be influential in the trajectories. We have
239 demonstrated its utility in an application to single cell transcriptomics involving external stimuli
240 and there is potential usage in high-throughput single cell CRISPR experiments that are as yet
241 unexplored [Adamson et al., 2016, Datlinger et al., 2017]. We also demonstrated applications to The
242 Cancer Genome Atlas using PhenoPath to model disease trajectories in colorectal and breast can-
243 cer. The trajectories identified were consistent are consistent with pre-existing knowledge concerning
244 tumorigenesis in these disease. Importantly, PhenoPath was able to identify covariate-pathway in-
245 teractions that might be driving specific trajectory differences recovering known associations as well
246 as novel genes. We showed that these behaviours cannot be readily determine with standard differ-
247 ential expression analyses without taking into account the latent disease progression. In summary,
248 PhenoPath provides a powerful and scalable pseudotime analysis algorithm for modelling latent pro-
249 gression in a variety of experimental settings. Future work will expand the ability of PhenoPath to
250 handle complex mixtures of continuous and discrete covariates in high-dimensional settings.

251 Methods

252 Statistical model

We begin with an $N \times G$ data matrix \mathbf{Y} where y_{ng} denotes the n^{th} entry in the g^{th} column for $n \in 1, \dots, N$ samples and $g \in 1, \dots, G$ features. Such a matrix would correspond to the measurement of a dynamic molecular process that we might reasonably expect to show continuous evolution such as gene expression corresponding to a particular pathway. It is then trivial to learn a one-dimensional linear embedding that would be our “best guess” of such progression via a factor analysis model:

$$y_{ng} = \lambda_g z_n + \epsilon_{ng}, \epsilon_{ng} \sim \mathcal{N}(0, \tau_g^{-1}) \quad (1)$$

253 where z_n is the latent measure of progression for sample n and λ_g is the factor loading for feature
254 g which essentially describes the evolution of g along the trajectory.

255 However, it is conceivable that the evolution of feature g along the trajectory is not identical for

256 all samples but is instead affected by a set of external covariates. Note that we expect such features
 257 to be “static” and should not correlate with the trajectory itself.

Introducing the $N \times P$ covariate matrix \mathbf{X} with the entry in the n^{th} row and p^{th} column given by x_{np} , we allow such measurements to perturb the factor loading matrix

$$\lambda_g \rightarrow \lambda_{ng} = \lambda_g + \sum_{p=1}^P \beta_{pg} x_{np} \quad (2)$$

where β_{pg} quantifies the effect of covariate p on the evolution of feature g . Despite \mathbf{Y} being column-centred we need to reintroduce gene and covariate specific intercepts to satisfy the model assumptions, giving a generative model of the form

$$y_{ng} = \eta_g + \sum_{p=1}^P \alpha_{pg} x_{np} + \left(\lambda_g + \sum_{p=1}^P \beta_{pg} x_{np} \right) z_n + \epsilon_{ng}, \quad \epsilon_{ng} \sim \text{N}(0, \tau_g^{-1}) \quad (3)$$

Our goal is inference of z_n that encodes progression along with β_{pg} which is informative of novel interactions between continuous trajectories and external covariates. Consequently we place a sparse Bayesian prior on β_{pg} of the form $\beta_{pg} \sim \text{N}(0, \chi_{pg}^{-1})$ where the posterior of χ_{pg} is informative of the model’s belief that β_{pg} is non-zero. The complete generative model is therefore given by

$$\begin{aligned} \alpha_{pg} &\sim \text{N}(0, \tau_\alpha^{-1}) \\ \lambda_g &\sim \text{N}(0, \tau_\lambda^{-1}) \\ z_n &\sim \text{N}(q_n, \tau_q^{-1}) \\ \beta_{pg} &\sim \text{N}(0, \chi_{pg}^{-1}) \\ \chi_{pg}^{-1} &\sim \text{Gamma}(a_\beta, b_\beta) \\ \tau_g^{-1} &\sim \text{Gamma}(a, b) \\ \mu_g &\sim \text{N}(0, \tau_\mu^{-1}) \\ \epsilon_{ng} &\sim \text{N}(0, \tau_g^{-1}) \\ y_{ng} &= \mu_g + \sum_p \alpha_{pg} x_{np} + \left(\lambda_g + \sum_p \beta_{pg} x_{np} \right) z_n + \epsilon_{ng} \end{aligned} \quad (4)$$

258 where $\tau_\alpha, \tau_\lambda, a, b, a_\beta, b_\beta, \tau_q$ are fixed hyperparameters and q_n encodes prior information about z_n
 259 if available but typically $q_n = 0 \forall i$ in the uninformative case.

To understand this model it helps to consider the distribution of \mathbf{Y} marginalised over the mapping $\{\lambda_g, \alpha_{pg}, \beta_{pg}\} \forall p, g$ with priors $\lambda_g \sim \text{N}(0, \tau_\lambda^{-1})$ and $\alpha_{pg} \sim \text{N}(0, \tau_\alpha^{-1})$. If \mathbf{y}_g denotes the column vectors of \mathbf{Y} and similarly \mathbf{x}_p for \mathbf{X} , $[\mathbf{z}]_n = z_n$, $\mathbf{1}_N$ is the column vector of ones and \odot denotes the

element-wise product, then

$$p(\mathbf{y}_g | \mathbf{X}, \mathbf{z}, \eta_g, \tau_g, \tau_\lambda, \tau_\alpha, \chi_{pg}) \sim \mathcal{N}(\eta_g \mathbf{1}_N, \boldsymbol{\Sigma}^{(g)}) \quad (5)$$

where

$$\boldsymbol{\Sigma}^{(g)} = \tau_g^{-1} \mathbf{1}_N \mathbf{1}_N^T + \tau_\alpha^{-1} \mathbf{X} \mathbf{X}^T + \tau_\lambda^{-1} \mathbf{z} \mathbf{z}^T + \sum_p \chi_{pg}^{-1} (\mathbf{x}_p \odot \mathbf{z})(\mathbf{x}_p \odot \mathbf{z})^T. \quad (6)$$

260 We therefore see that the addition of the covariates adds extra terms to the covariance matrix
 261 corresponding to *perturbations* of the latent variables with the covariates. Consequently, the scale
 262 on which \mathbf{x}_p is defined needs carefully calibrated. Furthermore, it is possible to extend the latent
 263 variable matrix to have dimension larger than 1 giving a novel dimensionality reduction technique
 264 for visualisation, though additional rotation issues arise.

265 Inference

We perform co-ordinate ascent mean field variational inference (see e.g. [Blei et al., 2016]) with an approximating distribution of the form

$$\begin{aligned} q & \left(\{z_n\}_{n=1}^N, \{\mu_g\}_{g=1}^G, \{\tau_g\}_{g=1}^G, \{\lambda_g\}_{g=1}^G, \{\alpha_{pg}\}_{g=1, p=1}^{G,P}, \{\beta_{pg}\}_{g=1, p=1}^{G,P}, \{\chi_{pg}\}_{g=1, p=1}^{G,P} \right) \\ & = \prod_{n=1}^N \underbrace{q_z(z_n)}_{\text{Normal}} \prod_{g=1}^G \underbrace{q_\mu(\mu_g)}_{\text{Normal}} \underbrace{q_\tau(\tau_g)}_{\text{Gamma}} \underbrace{q_\lambda(\lambda_g)}_{\text{Normal}} \prod_{p=1}^P \underbrace{q_\alpha(\alpha_{pg})}_{\text{Normal}} \underbrace{q_\beta(\beta_{pg})}_{\text{Normal}} \underbrace{q_\chi(\chi_{pg})}_{\text{Gamma}} \end{aligned} \quad (7)$$

Due to the model's conjugacy the optimal update for each parameter θ_j given all other parameters $\boldsymbol{\theta}_{-j}$ can easily be computed via

$$q_j^*(\theta_j) \propto \exp \{ \mathbf{E}_{-j} [\log p(\theta_j | \boldsymbol{\theta}_{-j}, \mathbf{X}, \mathbf{Y})] \} \quad (8)$$

266 where the expectation is taken with respect to the variational density over $\boldsymbol{\theta}_{-j}$.

267 Identifying significant interactions

268 For each gene g and covariate p we have β_{pg} that encodes the effect of p on the evolution of g along
 269 the trajectory \mathbf{z} . We would like to identify interesting or *significant* interactions for further analysis
 270 and follow up.

The variational approximation for β_{pg} is given by

$$q_{\beta_{pg}} \sim \mathcal{N}(m_{\beta_{pg}}, s_{\beta_{pg}}^2). \quad (9)$$

We therefore define an interaction as significant if 0 falls outside the posterior $n\sigma$ interval of

$m_{\beta_{pg}}$. In other words, the interaction between p and g is significant if

$$m_{\beta_{pg}} - n s_{\beta_{pg}} > 0 \quad (10)$$

or

$$m_{\beta_{pg}} + n s_{\beta_{pg}} < 0 \quad (11)$$

271 Note that variational inference typically underestimates posterior variances [Blei et al., 2016] so
272 such a designation of *significant* will be under-conservative. For all analyses we select $n = 3$, which
273 would loosely correspond to 0 being outside the 99.7% posterior interval of β_{pg} .

274 Synthetic data study

We performed a small simulation study to identify effects uncovered by PhenoPath that are missed by standard differential expression analyses. Specifically, we sought to compare differentially expressed genes identified by limma voom [Law et al., 2014], one of the leading RNA-seq differential expression methods, to the β interactions from PhenoPath. For $N = 200$ samples we assigned each to one of two categories given by the x values $x = -1, 1$, and assigned a pseudotime z through draws from a standard normal distribution. For each sample $i = 1, \dots, N$ and gene $g = 1, \dots, G$ we then generated a mean value through the PhenoPath mean function

$$\mu_{ig} = \alpha_g x_i + (c_g + \beta_g x_i) z_i \quad (12)$$

275 The gene-specific parameters (α_g, c_g, β_g) were sampled in equal proportions from one of four
276 classes:

- 277 1. *Differential expression only* where $\alpha_g = 1$ or -1 with equal probability and $c_g = \beta_g = 0$
- 278 2. *Pseudotime regulation only* where $c_g = 1$ or -1 with equal probability and $\alpha_g = \beta_g = 0$
- 279 3. *Pseudotime and covariate interactions* where c_g and β_g are set to 1 or -1 with equal probability
280 and $\alpha_g = 0$
- 281 4. *Differential expression, pseudotime and covariate interactions* where all parameters take on
282 values of -1 or 1 with equal probabilities

In order to generate RNA-seq reads we need positive count values. In the spirit of general linear models, we then used $g(x) = 2^x$ as a link function and generated a matrix of positive means

$$\tilde{\mu}_{ig} = 2^{\mu_{ig}} \quad (13)$$

283 We subsequently simulated a count matrix c_{ig} by sampling for each entry from a negative bi-
284 nomial distribution with mean $\tilde{\mu}_{ig}$ and size parameter $\tilde{\mu}_{ig}/3$. While this could be used as input
285 to PhenoPath (suitable log transformed), we sought to make our simulation as realistic as possible
286 including quantification errors. We subsequently simulated FASTA files using the Bioconductor
287 package `polyester` [Frazee et al., 2015] using the first 400 transcripts of the reference transcriptome
288 of the 22nd human chromosome. FASTA files were then converted to FASTQ files using a script
289 copied from StackOverflow and quantified into TPM and count estimates using Kallisto [Bray et al.,
290 2016]. The $\log_2(\text{TPM} + 1)$ values were then used for input to PhenoPath while the raw count values
291 were used for input to `limma voom`.

292 In our simulation study, Limma Voom “only” detects 47% of the genes simulated as differentially
293 expressed. Such power to detect differential expression is dependent on effect sizes and measurement
294 noise, and so such a figure is in no way unreasonable given the parameters used. While a more
295 comprehensive simulation study could examine detection rates across entire distributions over effect
296 sizes and measurement noise, we simply sought to perform a simulation that demonstrated that
297 PhenoPath identifies a subset of differential expression and that standard differential expression
298 misses some interactions across a consistent effect size and noise regime.

299 Fitting pseudotimes to Shalek et al. dataset

300 The Shalek et al. dataset of time-series dendritic cells was previously used in a pseudotime analysis
301 where the capture times were explicitly used as priors on the latent space [Reid and Wernisch, 2016].
302 However, in PhenoPath we provide no explicit temporal information, so sought to perform a brief
303 comparison to two popular pseudotime algorithms, Monocle 2 [Qiu et al., 2017] and DPT [Haghverdi
304 et al., 2016]. For both methods we provided the same normalised log expression (see section below)
305 and ran the algorithms with the default parameters. Performance of each algorithm was assessed
306 by regressing the inferred pseudotimes on the capture times using the R function `lm` and computing
307 the R^2 .

308 Data retrieval and processing

309 Shalek et al.

310 Preprocessed TPM values for all cells were retrieved from the Gene Expression Omnibus (GSE48968).
311 We retained cells treated by LPS and PAM at time points 1h, 2h, 4h, and 6h, resulting in 820 cells
312 (479 LPS and 341 PAM). We retained the 7533 genes whose variance in $\log_2(\text{TPM} + 1)$ expression
313 was greater than 2. The first principal component of the data showed a strong dependency on the
314 number of features expressed - previously been implicated in technical effects [Hicks et al., 2015]
315 - which we subsequently removed using the `normalizeExprs` function in `Scater` [McCarthy et al.,

316 2017].

317 TCGA studies

318 For both COAD and BRCA studies, TPM matrices were retrieved from a recent transcript-level
319 quantification of the entire TCGA study [Tatlow and Piccolo, 2016]. Clinical metadata, including
320 the phenotypic covariates used in PhenoPath, were retrieved using the RTCGA R package [Kosinski
321 and Biecek, 2016]. Transcript level expression estimates were combined to gene level expression
322 estimates using Scater [McCarthy et al., 2017].

323 Quality control and removal of samples

324 **COAD.** A PCA visualisation of the COAD dataset showed two distinct clusters based on the plate
325 of sequencing. Rather than try to correct such a large batch effect, we retained samples with a PC1
326 score of less than 0 and a PC3 score greater than -10, and removed any “normal” tumour types.
327 For input to PhenoPath we used the 4801 genes whose median absolute deviation in $\log(\text{TPM} + 1)$
328 expression was greater than $\sqrt{\frac{1}{2}}$.

329 **BRCA.** A PCA visualisation of the BRCA dataset showed a loosely dispersed outlier population
330 that separated on the first and third principal components. We performed Gaussian mixture model
331 clustering using the R package `mclust` [Fraley et al.], and removed samples designated as cluster 2
332 in the PCA plot, giving 1135 samples for analysis. For input to PhenoPath we used the 4579 genes
333 whose variance in $\log(\text{TPM} + 1)$ expression was greater than 1 and whose median absolute deviation
334 was greater than 0.

335 Identifying crossover points in BRCA

336 In PhenoPath we model gene expression evolving along the trajectories separately for each phenotype
337 (or covariate) considered. Unless the gradient of change along the trajectory is exactly equal for both
338 phenotypes (i.e. $\beta = 0$ exactly), the gene expression will cross at a given point in the trajectory.

339 Inference of this point would allow us to identify sections of the trajectory not affected by the
340 covariate and consequently sections of the trajectory that are. This is important as if the crossover
341 point occurs towards the beginning of the trajectory, it would mean gene expression is similar at
342 the beginning but diverges as we move along the trajectory. Similarly, if the crossover points occur
343 towards the end of the trajectory, it would imply the expression profiles for the two phenotypes
344 are different at the beginning of the trajectory, but converge as the trajectory progresses. An
345 interpretation of this would be that the effect on expression from the trajectory slowly dominates
346 over the effect of phenotypes on the trajectory.

347 It is important to note that the latent trajectory values loosely follow a $N(0, 1)$ distribution.

348 This means the ‘middle’ of the trajectory is any value around zero, values of -1 or less could be
349 thought of as the ‘beginning’ while values greater than 1 may be thought of as the ‘end’. Crucially,
350 we can derive an analytical expression from the PhenoPath parameters for the crossover point z^*
351 (see below).

352 We fitted the crossover points z^* for all *significant* genes in the BRCA dataset. We find that
353 the vast majority of the crossover times z^* occur towards the end of the trajectory, with a median
354 value of around 0.4. In other words, at the beginning of the trajectory most genes are differentially
355 expressed based on ER status, while as the trajectory progresses it comes to dominate at the gene
356 expression converges.

357 Inference of convergence point

The condition for the crossover point is that the predicted expression for each phenotype is identical.
Therefore (in the context of BRCA cancer)

$$y_g^{\text{ER}+}(z_g^*) = y_g^{\text{ER}-}(z_g^*) \quad (14)$$

which leads to the condition

$$\alpha_g x_{\text{ER}+} + (c_g + \beta_g x_{\text{ER}+}) z_g^* = \alpha_g x_{\text{ER}-} + (c_g + \beta_g x_{\text{ER}-}) z_g^* \quad (15)$$

which is in turn solved by

$$z_g^* = -\frac{\alpha_g}{\beta_g}. \quad (16)$$

358 References

359 References

- 360 Britt Adamson, Thomas M Norman, Marco Jost, Min Y Cho, James K Nuñez, Yuwen Chen, Jacque-
361 line E Villalta, Luke A Gilbert, Max A Horlbeck, Marco Y Hein, et al. A multiplexed single-cell
362 crispr screening platform enables systematic dissection of the unfolded protein response. *Cell*, 167
363 (7):1867–1882, 2016.
- 364 David M Blei, Alp Kucukelbir, and Jon D McAuliffe. Variational inference: A review for statisticians.
365 *arXiv preprint arXiv:1601.00670*, 2016.
- 366 C R Boland and A Goel. Microsatellite instability in colorectal cancer. *Gastroenterology*, 2010.
- 367 Valérie Bonadona, Bernard Bonaiti, Sylviane Olschwang, Sophie Grandjouan, Laetitia Huiart,
368 Michel Longy, Rosine Guimbaud, Bruno Buecher, Yves-Jean Bignon, Olivier Caron, Chrystelle

- 369 Colas, Catherine Noguès, Sophie Lejeune-Dumoulin, Laurence Olivier-Faivre, Florence Polycarpe-
370 Osaer, Tan Dat Nguyen, Françoise Desseigne, Jean-Christophe Saurin, Pascaline Berthet, Do-
371 minique Leroux, Jacqueline Duffour, Sylvie Manouvrier, Thierry Frébourg, Hagay Sobol, Christine
372 Lasset, Catherine Bonaïti-Pellié, and French Cancer Genetics Network. Cancer risks associated
373 with germline mutations in MLH1, MSH2, and MSH6 genes in lynch syndrome. *JAMA*, 305(22):
374 2304–2310, 8 June 2011.
- 375 Nicolas L Bray, Harold Pimentel, Páll Melsted, and Lior Pachter. Near-optimal probabilistic RNA-
376 seq quantification. 34(5):525–527, May 2016.
- 377 Kieran R Campbell and Christopher Yau. Order under uncertainty: robust differential expression
378 analysis using probabilistic models for pseudotime inference. *PLOS Computational Biology*, 12
379 (11):e1005212, 2016.
- 380 Paul Datlinger, André F Rendeiro, Christian Schmidl, Thomas Krausgruber, Peter Traxler, Johanna
381 Klughammer, Linda C Schuster, Amelie Kuchler, Donat Alpar, and Christoph Bock. Pooled crispr
382 screening with single-cell transcriptome readout. *Nature Methods*, 2017.
- 383 Chenfang Dong, Tingting Yuan, Yadi Wu, Yifan Wang, Teresa WM Fan, Sumitra Miriyala, Yiwei
384 Lin, Jun Yao, Jian Shi, Tiebang Kang, et al. Loss of fbp1 by snail-mediated repression provides
385 metabolic advantages in basal-like breast cancer. *Cancer Cell*, 23(3):316–331, 2013.
- 386 Early Breast Cancer Trialists’ Collaborative Group (EBCTCG). Relevance of breast cancer hormone
387 receptors and other factors to the efficacy of adjuvant tamoxifen: patient-level meta-analysis of
388 randomised trials. *Lancet*, 378(9793):771–784.
- 389 Andrea Facciabene, Gregory T Motz, and George Coukos. T-regulatory cells: key players in tumor
390 immune escape and angiogenesis. *Cancer Research*, 72(9):2162–2171, 2012.
- 391 Jean Fan, Neeraj Salathia, Rui Liu, Gwendolyn E Kaeser, Yun C Yung, Joseph L Herman, Fiona
392 Kaper, Jian-Bing Fan, Kun Zhang, Jerold Chun, et al. Characterizing transcriptional hetero-
393 geneity through pathway and gene set overdispersion analysis. *Nature Methods*, 13(3):241–244,
394 2016.
- 395 Napoleone Ferrara. Vegf and the quest for tumour angiogenesis factors. *Nature Reviews Cancer*, 2
396 (10):795–803, 2002.
- 397 C Fraley, A E Raftery, T B Murphy, and L Scrucca. mclust version 4 for r: Normal mixture modeling
398 for Model-Based clustering, classification, and density estimation. 2012. *University of Washington:*
399 *Seattle*.

- 400 Alyssa C Frazee, Andrew E Jaffe, Ben Langmead, and Jeffrey T Leek. Polyester: simulating RNA-seq
401 datasets with differential transcript expression. *Bioinformatics*, 31(17):2778–2784, 1 September
402 2015.
- 403 J J P Gille, F B L Hogervorst, G Pals, J Th Wijnen, R J van Schooten, C J Dommering, G A
404 Meijer, M E Craanen, P M Nederlof, D de Jong, C J McElgunn, J P Schouten, and F H Menko.
405 Genomic deletions of MSH2 and MLH1 in colorectal cancer families detected by a novel mutation
406 detection approach. *Br. J. Cancer*, 87(8):892–897, 7 October 2002.
- 407 Anupam Gupta and Ziv Bar-Joseph. Extracting dynamics from static cancer expression data.
408 *IEEE/ACM Transactions on Computational Biology and Bioinformatics*, 5(2):172–182, 2008.
- 409 Laleh Haghverdi, Maren Büttner, F Alexander Wolf, Florian Buettner, and Fabian J Theis. Diffusion
410 pseudotime robustly reconstructs lineage branching. *Nat. Methods*, 13(10):845–848, October 2016.
- 411 S C Hicks, M Teng, and R A Irizarry. On the widespread and critical impact of systematic bias and
412 batch effects in single-cell RNA-Seq data. *bioRxiv*, 2015.
- 413 Marcin Kosinski and Przemyslaw Biecek. *RTCGA: The Cancer Genome Atlas Data Integration*,
414 2016. URL <https://rtcga.github.io/RTCGA>. R package version 1.4.0.
- 415 Eric W-F Lam, Jan J Brokens, Ana R Gomes, and Chuay-Yeng Koo. Forkhead box proteins: tuning
416 forks for transcriptional harmony. *Nature Reviews Cancer*, 13(7):482–495, 2013.
- 417 Charity W Law, Yunshun Chen, Wei Shi, and Gordon K Smyth. voom: Precision weights unlock
418 linear model analysis tools for RNA-seq read counts. *Genome Biol.*, 15(2):R29, 3 February 2014.
- 419 Paul M Magwene, Paul Lizardi, and Junhyong Kim. Reconstructing the temporal ordering of
420 biological samples using microarray data. *Bioinformatics*, 19(7):842–850, 2003.
- 421 Davis J McCarthy, Kieran R Campbell, Aaron T L Lun, and Quin F Wills. Scater: pre-processing,
422 quality control, normalization and visualization of single-cell RNA-seq data in R. *Bioinformatics*,
423 14 January 2017.
- 424 S Michel, A Benner, M Tariverdian, N Wentzensen, P Hoefler, T Pommerencke, N Grabe, M von
425 Knebel Doeberitz, and M Kloor. High density of foxp3-positive t cells infiltrating colorectal cancers
426 with microsatellite instability. *British journal of cancer*, 99(11):1867–1873, 2008.
- 427 Cancer Genome Atlas Network et al. Comprehensive molecular characterization of human colon and
428 rectal cancer. *Nature*, 487(7407):330–337, 2012.
- 429 F F Parl, B P Schmidt, W D Dupont, and R K Wagner. Prognostic significance of estrogen receptor
430 status in breast cancer in relation to tumor stage, axillary node metastasis, and histopathologic
431 grading. *Cancer*, 54(10):2237–2242, 15 November 1984.

- 432 Peng Qiu, Andrew J Gentles, and Sylvia K Plevritis. Discovering biological progression underlying
433 microarray samples. *PLoS Comput Biol*, 7(4):e1001123, 2011.
- 434 Xiaojie Qiu, Andrew Hill, Jonathan Packer, Dejun Lin, Yi-An Ma, and Cole Trapnell. Single-cell
435 mRNA quantification and differential analysis with census. *Nat. Methods*, 14(3):309–315, March
436 2017.
- 437 John E Reid and Lorenz Wernisch. Pseudotime estimation: deconfounding single cell time series.
438 *Bioinformatics*, 32(19):2973–2980, 1 October 2016.
- 439 Manu Setty, Michelle D Tadmor, Shlomit Reich-Zeliger, Omer Angel, Tomer Meir Salame, Pooja
440 Kathail, Kristy Choi, Sean Bendall, Nir Friedman, and Dana Pe’er. Wishbone identifies bifurcating
441 developmental trajectories from single-cell data. *Nature biotechnology*, 34(6):637–645, 2016.
- 442 Alex K Shalek, Rahul Satija, Joe Shuga, John J Trombetta, Dave Gennert, Diana Lu, Peilin Chen,
443 Rona S Gertner, Jellert T Gaublomme, Nir Yosef, Schraga Schwartz, Brian Fowler, Suzanne
444 Weaver, Jing Wang, Xiaohui Wang, Ruihua Ding, Raktima Raychowdhury, Nir Friedman, Nir
445 Hacohen, Hongkun Park, Andrew P May, and Aviv Regev. Single-cell RNA-seq reveals dynamic
446 paracrine control of cellular variation. *Nature*, 510(7505):363–369, 19 June 2014.
- 447 P J Tatlow and Stephen R Piccolo. A cloud-based workflow to quantify transcript-expression levels
448 in public cancer compendia. *Sci. Rep.*, 6:39259, 16 December 2016.
- 449 Cole Trapnell, Davide Cacchiarelli, Jonna Grimsby, Prapti Pokharel, Shuqiang Li, Michael Morse,
450 Niall J Lennon, Kenneth J Livak, Tarjei S Mikkelsen, and John L Rinn. The dynamics and
451 regulators of cell fate decisions are revealed by pseudotemporal ordering of single cells. *Nature*
452 *Biotechnology*, 32(4):381–386, 2014.
- 453 Allan Tucker and David Garway-Heath. The pseudotemporal bootstrap for predicting glaucoma from
454 cross-sectional visual field data. *IEEE Transactions on Information Technology in Biomedicine*,
455 14(1):79–85, 2010.
- 456 Allan Tucker and Yuanxi Li. Updating stochastic networks to integrate cross-sectional and longi-
457 tudinal studies. In *Conference on Artificial Intelligence in Medicine in Europe*, pages 113–122.
458 Springer, 2015.
- 459 Allan Tucker, Yuanxi Li, Stefano Ceccon, and Stephen Swift. Trajectories through the disease
460 process: Cross sectional and longitudinal studies. In *Foundations of Biomedical Knowledge Rep-
461 resentation*, pages 189–205. Springer, 2015.
- 462 Allan Tucker, Yuanxi Li, and David Garway-Heath. Updating markov models to integrate cross-
463 sectional and longitudinal studies. *Artificial Intelligence in Medicine*, 77:23–30, 2017.

Supplementary Table 1: A comparison of true positive, false positive, and false discovery rates for Limma Voom detecting differential expression and PhenoPath detecting covariate-pseudotime interactions on synthetic data.

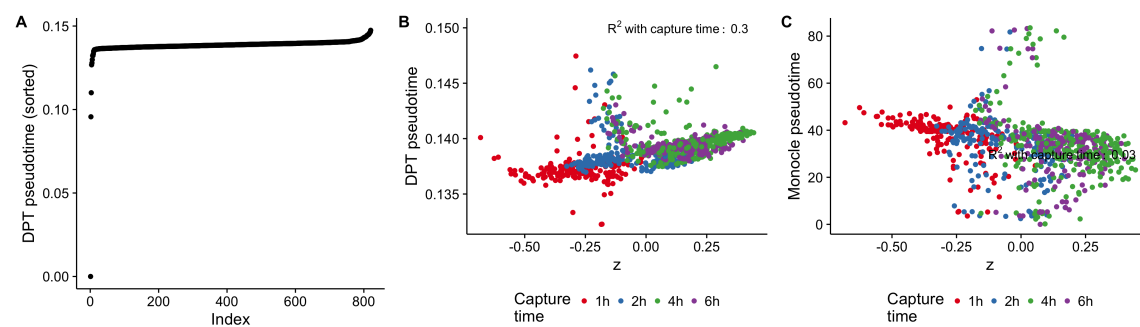
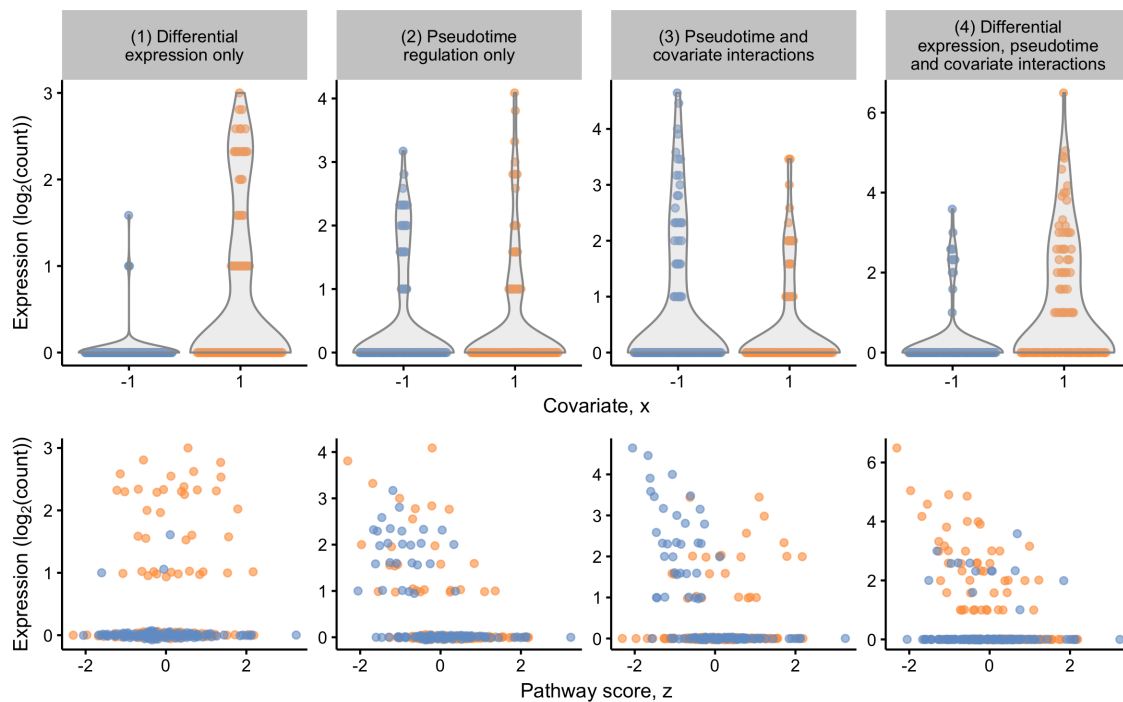
Algorithm	True positive rate	False positive rate	False discovery rate
Limma Voom	0.82	0.09	0.18
PhenoPath	0.97	0.02	0.03

464 Jonathan Welte, Sonja Loges, Stefanie Dimmeler, and Peter Carmeliet. Recent molecular discoveries
465 in angiogenesis and antiangiogenic therapies in cancer. *The Journal of Clinical Investigation*, 123
466 (8):3190–3200, 2013.

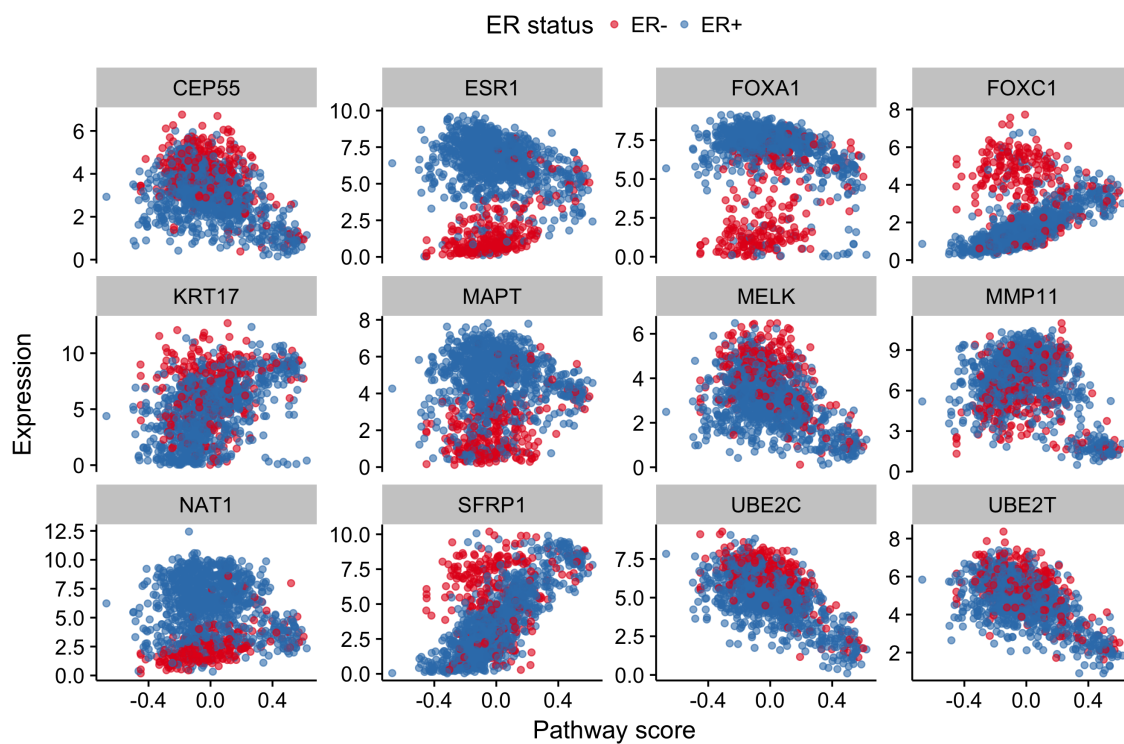
467 Yi Yu-Rice, Yanli Jin, Bingchen Han, Ying Qu, Jeffrey Johnson, Takaaki Watanabe, Long Cheng,
468 Nan Deng, Hisashi Tanaka, Bowen Gao, et al. Foxc1 is involved in $er\alpha$ silencing by counteracting
469 gata3 binding and is implicated in endocrine resistance. *Oncogene*, 2016.

470 Acknowledgements

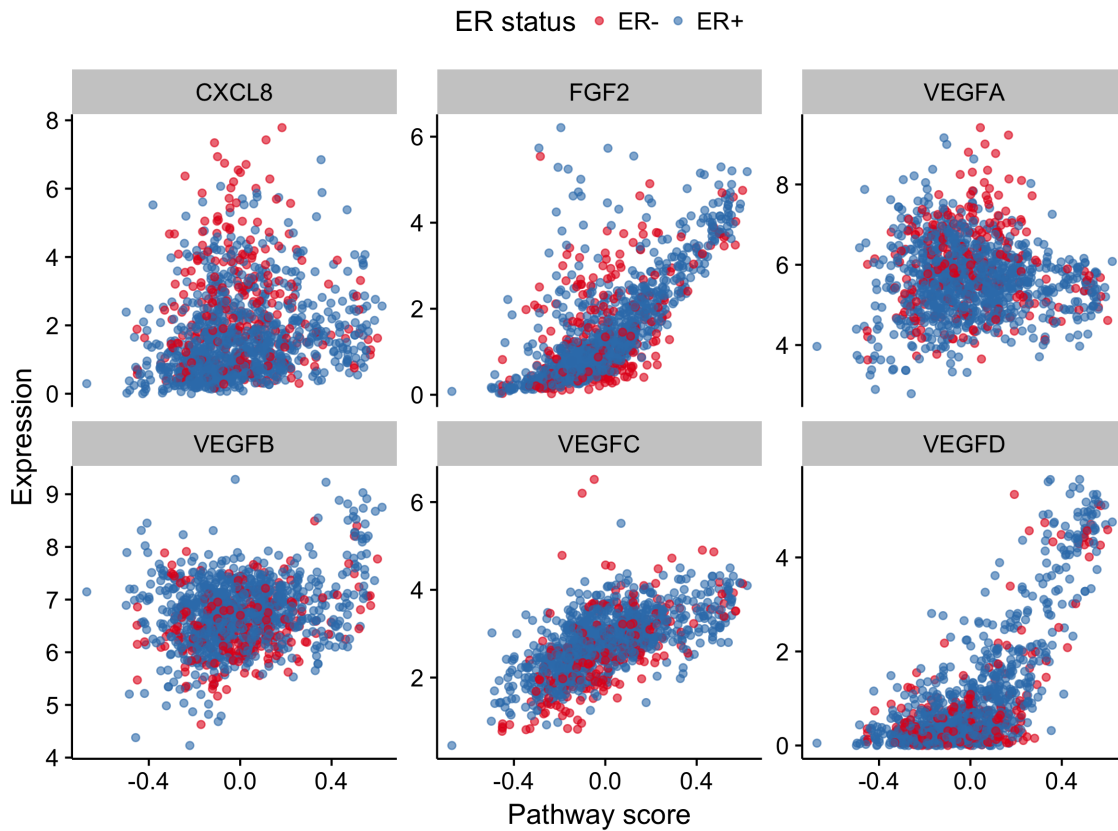
471 K.C. is supported by a UK Medical Research Council funded doctoral studentship. C.Y. is supported
472 by a UK Medical Research Council New Investigator Research Grant (Ref. No. MR/L001411/1)
473 and Methodology Research Grant (MR/P02646X/1) and the Wellcome Trust Core Award Grant
474 Number 090532/Z/09/Z.



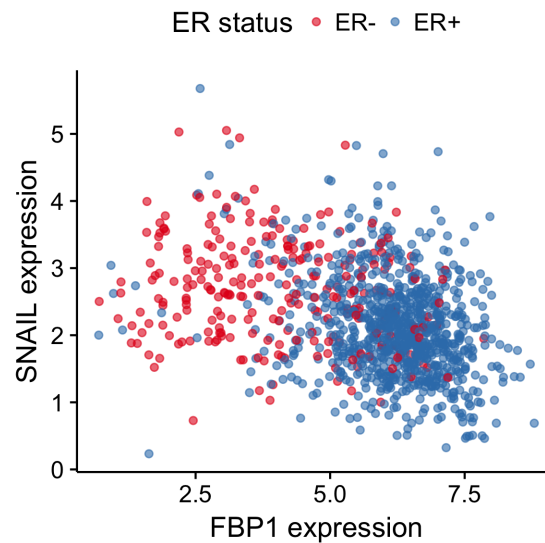
Supplementary Figure 2: Performance of DPT and Monocle 2 on Shalek et al dataset. **A** Sorted DPT pseudotimes by index identifies three outlier cells. **B** Comparison of DPT pseudotimes to PhenoPath pathway score z . **C** Comparison of Monocle 2 pseudotimes to PhenoPath pathway score z .



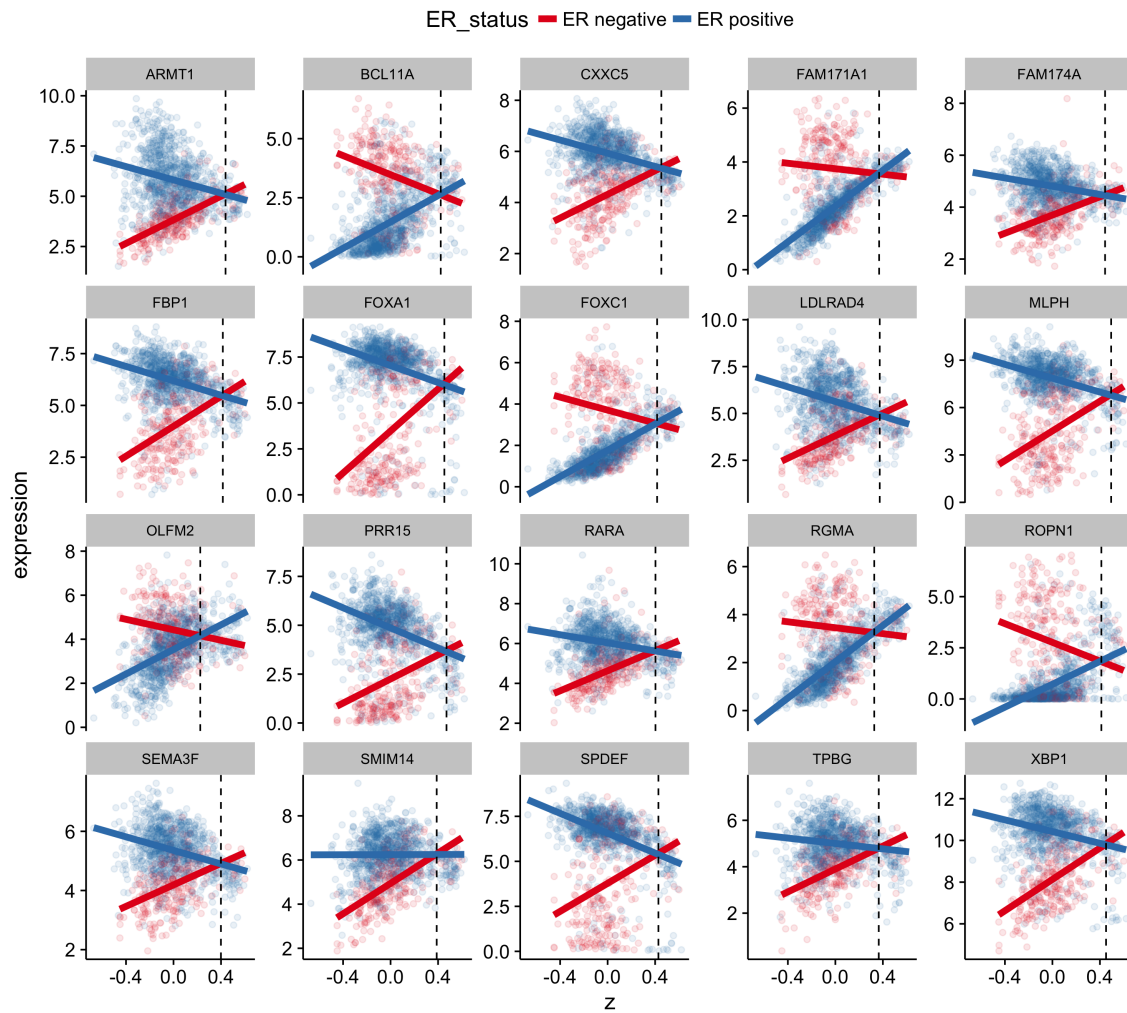
Supplementary Figure 3: Pseudotemporally ordered gene expression trajectories for the TCGA Breast Cancer data for 12 breast cancer-associated genes.



Supplementary Figure 4: Pseudotemporally ordered gene expression trajectories for the TCGA Breast Cancer data for six angiogenesis-associated genes.



Supplementary Figure 5: FBP1 expression is inversely correlated with Snail in ER- breast cancers but shows no dependence in ER+ breast cancers.



Supplementary Figure 6: Expression of 20 genes with the largest interaction effects along the inferred pseudotemporal trajectory coloured by estrogen receptor status with linear fits as solid lines. The vertical dashed line indicates the crossover point.